JOURNAL OF CATALYSIS **167,** 482–494 (1997)
ARTICLE NO. CA971604

Structure and Characterization of Supported Ruthenium–Cobalt Bimetallic Catalysts

L. Guczi,*,[1] R. Sundararajan,* Zs. Koppány,* Z. Zsoldos,* Z. Schay,* F. Mizukami,† and S. Niwa†

*Department of Surface Chemistry and Catalysis, Institute of Isotopes of the Hungarian Academy of Sciences, P.O. Box 77, H-1525 Budapest, Hungary; and †National Institute of Materials and Chemical Research, 1-1 Higashi, Tsukuba, Ibaraki 305, Japan

Received July 3, 1996; revised October 25, 1996; accepted January 3, 1997

Ruthenium, cobalt, and ruthenium–cobalt bimetallic samples, supported on SiO_2, Al_2O_3, and NaY zeolite, were characterized by temperature-programmed reduction, CO chemisorption, X-ray diffraction, X-ray photoelectron spectroscopy, and transmission electron microscopy. Temperature-programmed reduction revealed that the reducibility for cobalt increases in the order NaY < SiO_2 < Al_2O_3, while for ruthenium the sequence was Al_2O_3 < NaY < SiO_2. If Ru/NaY samples are calcined in oxygen, then ruthenium migrates to the external surface of NaY and agglomerates, while in the case of He-treated zeolite samples the ruthenium metal particles are stabilized in the supercage in the range of 1 to 3 nm average diameter, as measured by X-ray diffraction, CO chemisorption, and transmission electron microscopy. Cobalt ions are irreducible when they are exchanged alone or first in the NaY zeolite for the bimetallic sample Ru–Co/NaY[I]. Here the reduction of Ru^{3+} ions is not affected by the presence of cobalt, whereas when Ru^{3+} ions exchanged first into NaY (Ru–Co/NaY[II]), the cobalt ions are easily reduced and bimetallic particles are formed but the migration of ruthenium particles to the outer surface of NaY zeolite is hampered.

1. INTRODUCTION

Oxidative coupling of methane (OCM) could be an interesting alternative route for the production of ethane in spite of the drawbacks such as low conversion, requirement of high temperature, and formation of CO_2 as a by-product (1). Low-temperature methane activation under nonoxidative conditions has been the subject of wide-scale investigations during the past few years (2–6). In this "two-step reaction" first methane is chemisorbed on a catalyst, and in the second stage, the chemisorbed methane is removed by a stream of hydrogen at low temperature to form higher molecular weight hydrocarbons. Although the two-step reaction overcomes difficulties of OCM, the thermodynamics for this process is very unfavorable. The dissociative methane chemisorption requires high temperature (2) and at this temperature the carbon species are easily transformed into nonreactive carbonaceous entities (3).

C–H bond activation in methane has also been extensively investigated by Solymosi and co-workers wherein exceptional activity of platinum, palladium, rhodium, and iridium metals supported by various inorganic oxides was observed (7–9). Surface science studies also showed the stability of CH_3 or CH_2 formed on a Pd(100) surface (10–12) and on Pt(111) (13). Platinum also proved to be an excellent catalyst (14), if is encaged in the NaY zeolite and compared to other platinum-containing catalysts, e.g., EUROPt-1 (15–18). The temperature of methane chemisorption and that of sequential hydrogenation to remove the hydrocarbons produced could be lowered to 250°C. Conversion of the CH_x species (denoted as the surface species formed from methane), chemisorbed on the platinum surface, into higher hydrocarbons was quite high due to the stabilization of metal particles inside the zeolite supercages. The yield could be increased significantly if the hydrogen formed is removed continuously during methane dissociative chemisorption (16).

Silica-supported cobalt and ruthenium were suggested to be active in methane activation and homologation (2, 4, 18, 19); and their activity could be significantly improved by pretreating the Ru/SiO_2 with CO (20) or by adding of vanadium (21). The major drawback of cobalt and ruthenium catalysts is the high temperature used for methane dissociative chemisorption to occur, but this difficulty could be overcome by inserting these metals into a zeolite matrix. For instance, platinum–cobalt particles, inserted into a NaY zeolite supercage, were developed as a new catalyst (22–25) and proved to be highly active and selective in converting chemisorbed methane into higher hydrocarbons (yield and selectivity) over Pt/NaY catalysts (26).

Preliminary experiments have shown that catalytic activity in methane dissociative chemisorption can be affected by the structure of the metallic sites (particle size and oxidation state). Conversely, both the reduction and the size of the metal components are functions of the metal support interaction as well as of the presence of the second metal.

[1] To whom correspondence should be addressed. Fax: +361-395-9001. E-mail: guczi@alpha0.iki.kfki.hu.

0021-9517/97 $25.00

Our experiments have shown (27, 28) that the performance of cobalt and ruthenium in the two-step process was also enhanced by inserting them into NaY zeolite matrix. Similar results was obtained for the Rh–Cu/SiO_2 sample revealed an enhanced ethane formation (29).

The present paper reports on the effect of support (silica, alumina, and NaY) as well as the creation of bimetallic particles. Earlier studies (30–35) reported migration of ruthenium from the exchanged NaY matrix to the external surface and the stability of small ruthenium particles under different conditions. We are, therefore, especially interested in the genesis of metal and bimetallic particles in the zeolite-supported ruthenium and cobalt samples and in how the sequence of ion exchange and the pretreatment conditions affect the structure of the metal particles formed. Temperature-programmed reduction, X-ray diffraction, X-ray photoelectron spectroscopy, transmission electron microscopy, and CO chemisorption were used for characterizing the metal particles.

2. EXPERIMENTAL

2.1. Catalyst Preparation

The alumina- and silica-supported catalyst samples were prepared by incipient wetness of alumina and silica using aqueous solutions of $Ru(NH_3)_6Cl_3$ and $Co(NO_3)_2$. The samples were dried at 100°C, calcined at 300°C for 2 h in a stream of oxygen, and then reduced at 450°C for 2 h in a stream of hydrogen. Bimetallic samples were prepared by co-impregnation using the solution of both precursors.

Co/NaY, Ru–Co/NaY, and Ru/NaY samples were prepared by ion exchange of NaY zeolite (Strem Chemicals, Lot No. 031112104). The zeolite support was first stirred carefully with deionized water (200 $cm^3/g_{zeolite}$) at 100°C for 1 h and a diluted aqueous solution of $Ru(NH_3)_6Cl_3$ or $Co(NO_3)_2$ (2×10^{-3} mol/cm^3) was added dropwise to the zeolite slurry while stirring at 70°C. The pH of the slurry was set to a final value of 6.5. After 24 h ion exchange at the same temperature, the samples were filtered and thoroughly washed with deionized water. Two types of Ru–Co/NaY bimetallic catalysts were prepared. In the first type of sample denoted Ru–Co/NaY[**I**], first $Co(NO_3)_2$ and then $[Ru(NH_3)_6]Cl_3$ were introduced, while in the second type of catalysts, denoted Ru–Co/NaY[**II**], the sequence of exchange was reversed.

The exchange process was followed by determinations of the Na1*s*/Si2*p* ratio as measured by XPS (25). In the present case the Na/Si ratios are 0.72, 0.26, 0.16, and 0.6 for NaY, Ru/NaY, Ru–Co/NaY[**I**], and Ru–Co/NaY[**II**], respectively. All materials were dried in air for 2 h, first at room temperature and then at 110°C.

The metal content of the ruthenium and cobalt samples was determined by X-ray fluorescence (Table 1). The bulk atomic ratio of the pure NaY zeolite was Na/Al/Si = 0.38/0.38/1.00. The percentage exchange for the various samples is in the range of 30–50%.

TABLE 1

Metal Loading of the Various Catalysts Analyzed by X-Ray Fluorescence

Elements: Support	Ru	Co	Ru–Co		Ru–Co/NaY[**I**]		Ru–Co/NaY[**II**]	
			Ru	Co	Ru	Co	Ru	Co
SiO_2	2.5	3.2	2.6	1.7				
Al_2O_3	3.5	5.3						
NaY	4.1	2.4			3.4	1.7	3.8	2.8
Exchange (%)	30	20			40		50	

The preliminary experiments and literature data (27, 28, 35–38) for calcination in oxygen indicated that ruthenium migrates to the external surface of zeolite; the decomposition of the ruthenium complex was therefore carried out in He (40 cm^3/min). Reduction of the samples was carried out in a stream of H_2 (40 cm^3/min) increasing the temperature to 450°C, keeping the sample at this temperature for 1 h, and then cooling to room temperature.

2.2. Catalyst Characterization

X-ray diffraction was carried out in a Philips X-ray diffractometer equipped with a CuK_α source using a Guinier camera.

Temperature-programmed reduction (TPR) as well as CO chemisorption were measured in a SORBSTAR pulse-flow system equipped with a thermal conductivity detector and quadrupole mass spectrometer, respectively. In all measurements 100 mg of sample was placed in a U-tube and, after the necessary pretreatment (calcination or treatment in He), high-purity argon gas passed through the tube at a flow rate of 15 cm^3/min. In all cases a 10°C/min temperature ramp rate was used. One volume percent of hydrogen in argon and CO pulse in He was applied for TPR and CO chemisorption, respectively.

XPS measurements were carried out in a KRATOS ES-300 type ESCA machine using AlK_α, line with 225 W power. The slits were adjusted to achieve the best resolution, and the base pressure never exceeded 10^{-6} Pa. A paste of the aqueous suspension of the catalyst powder was placed on the sample holder. The binding energy (B.E.) scale was referenced to Si2p = 102.7 eV and to Al2p = 73.7 eV for NaY- and Al_2O_3-supported samples, respectively. Due to overlapping of the Ru3*d* and C1*s* lines, the Ru3*p* line was used. The O1*s* Auger line is known to appear at similar binding energy as Ru3*p*. Since a large quantity of oxygen was present, the intensity data of the Ru3*p* peak was corrected for oxygen Auger contribution (corrected with O1*s* K_β). During spectra recording the hemispherical analyzer worked in fixed retarding ratio mode.

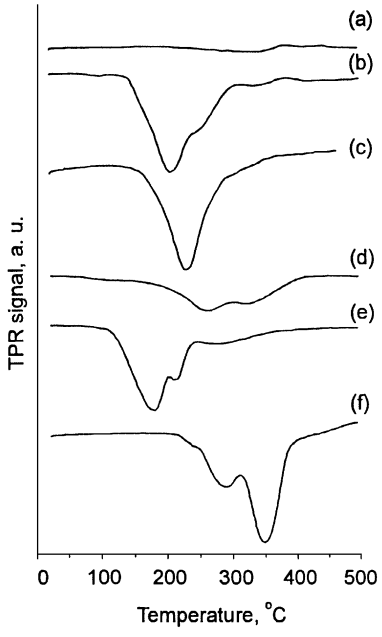

FIG. 1. Temperature-programmed reduction of silica-supported catalysts. (a) Co/SiO_2; (b) $Co–Ru/SiO_2$; and (c) Ru/SiO_2. Alumina-supported catalysts: (d) Co/Al_2O_3; (e) $Co–Ru/Al_2O_3$; and (f) Ru/Al_2O_3.

The genesis of the metallic sites in the various samples was investigated in the sequence of as-received state (the term is used for the sample after ion exchange) after drying, after sample calcination in He and/or O_2, and after sample reduction. Sample treatments were carried out *in situ*, in a small pretreatment cell directly attached to the UHV chamber of the ESCA machine, or *ex situ*. In the *in situ* procedure the sample was transferred to analysis position without being exposed to air. A series of experiments was carried out in XSAM800cpi ESCA machine (KRATOS) for Ru–Co/NaY[**II**] sample, using *in situ* treatment for the sample. Unless otherwise stated, treatment in He was carried out at 300°C for 1 h, calcination/oxidation in O_2 was carried out at 300°C for 2 h, and reduction in H_2 was carried out at 450°C for 2 h. The accuracy of binding energy determination is ± 0.1 eV.

A JEOL FX2000 type transmission electron microscope was used to obtain high-resolution TEM pictures of the Ru/NaY and Ru–Co/NaY[**II**] samples after hydrogen treatment at 450°C for 2 h.

3. RESULTS

3.1. Temperature-Programmed Reduction and CO Chemisorption

Since methane activation requires metallic sites two problems will be addressed in this section: (i) the degree of reduction of the metal ions present in the precursor (defined by the fraction of metal ions transformed into metal particles and calculated from the hydrogen uptake measured in TPR) and (ii) formation of the bimetallic particles and the understanding of their stability.

The TPR curves for the silica-supported (Co/SiO_2, Ru/SiO_2, and $Ru–Co/SiO_2$), alumina-supported (Co/Al_2O_3, Ru/Al_2O_3, and $Ru–Co/Al_2O_3$), and NaY-supported catalysts (Ru/NaY, Co/NaY, Ru–Co/NaY[**I**], and Ru–Co/NaY[**II**]) are presented in Figs. 1 and 2. Reducibility of various metals on different supports can be characterized by the degree of reduction and/or by a shift in the reduction peak. These data are presented in Table 2.

Table 2, column 4, gives the degree of reduction calculated from the H_2 uptake presented in column 3. Column 5 represents the number of CO molecules in micromoles per gram of catalyst chemisorbed at room temperature and from this the metal dispersion was calculated (column 6). In the last column T_{max} values are presented as measured by TPR (a minimum in the gas phase hydrogen concentration plotted in the TPR curves).

Temperature-programmed reduction (characterized by T_{max}) of silica- and alumina-supported cobalt and ruthenium samples is presented in Fig. 1. The degree of cobalt reduction in the Co/SiO_2 sample was very low, probably due to cobalt silicate formation (39), while Ru^{3+} ions in both the Ru/SiO_2 and the $Ru–Co/SiO_2$ samples were easily reduced.

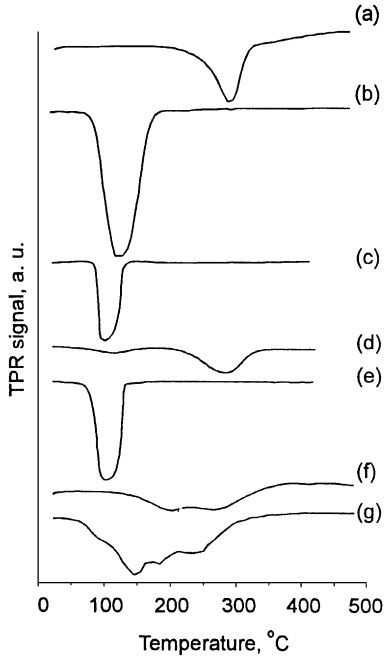

FIG. 2. Temperature-programmed reduction of various samples. Ru/NaY: (a) after He treatment; (b) oxygen treatment after (a). Co–Ru/NaY[**I**]: (c) after He treatment; (d) oxygen treatment after (c); and (e) direct oxidation. Ru–Co/NaY[**II**]: (f) after He treatment; (g) oxygen treatment after (f).

TABLE 2

Hydrogen TPR Data, CO Chemisorption, Dispersion (D), and T_{max} on Various Samples

Sample	Treatment	H_2 uptake (μmol/g_{cat})	Extent of reduction[a]	CO (ads) (μmol/g_{cat})	D (%)	T_{max} (°C)
Co/SiO_2	O_2	31	0.06	NA	—	330
Ru/SiO_2	O_2	421	1.13	NA	—	230
$Ru–Co/SiO_2$	O_2	472	0.7	NA	—	206
Co/Al_2O_3	O_2	275	0.3	29	14	261
Ru/Al_2O_3	O_2	574	1.1	32	9	352
$Ru–Co/Al_2O_3$	O_2	402	0.25	16	5	180
$Ru–Co/Al_2O_3$	He	261	0.16	64	30	227
Co/NaY	He	39	0.1	28	68	607
Ru/NaY	He	330	0.54	240	100	287
	O_2 after He	661	1.08	<5		120
	O_2 direct	630	1.1	Nil	—	117
Ru–Co/ NaY[**I**]	He	294	0.37	180	77	124, 310
	O_2 after He	571	0.72	52	11	111
	O_2 direct	675	0.85	42	8	106
Ru–Co/ NaY[**II**]	He	324	0.31	150	56	200
	O_2 after He	630	0.61	120	27	145

[a] Ratio of measured and calculated hydrogen uptake.

The latter had the lowest T_{max}, which might be the result of a weaker interaction between the silica and ruthenium due to the formation of CoO/SiO_2 interface.

On alumina the state of the cobalt and ruthenium ions was somewhat different, as illustrated in Fig. 1. Although ruthenium is still fully reducible (but at a higher temperature on alumina than on silica), only some of the Co^{2+} ions were reduced due to the cobalt surface phase (CSP) formation (40–42). On the other hand, in the presence of CSP the strong ruthenium/alumina interaction did not exist; T_{max} in the reduction of Ru^{3+} ions was lowered. When the bimetallic sample was decomposed in He, a slight increase in T_{max} (not shown in Fig. 1) with a simultaneous increase in CO chemisorption was observed, consequently in metal disperison.

The most interesting feature is given by the NaY-supported samples (Fig. 2). Reduction of Co/NaY proceeds to a negligible extent (not shown in Fig. 2), even above 600°C as was found in earlier studies (22, 23). However, the extent of reduction of Ru^{3+} ions in Ru/NaY was 0.54–0.64 and the CO chemisorption is 240 μmol/g_{cat} (see Fig. 1, curve a).

Subsequent calcination in oxygen results in a shift of T_{max} from 300°C to around 120°C as well as a simultaneous increase in the hydrogen uptake and a narrower TPR peak (Fig. 1, curve b). The amount of hydrogen uptake indicated a full reduction of the RuO_2 particles of a 100 nm in average diameter measured by XRD. After reduction the ruthenium metal particles did not change. Due to the large metal particles the CO chemisorption drastically decreases (see Table 2 and compare rows 8 and 9).

The TPR curve for the Ru–Co/NaY[**I**] sample (curve d) was not similar to that of Ru/NaY. Surprisingly, the TPR spectrum showed two peaks (T_{max} = 124 and 310°C) the first being at 124°C that was characteristic of large particles. This pointed to the migration of ruthenium to the external surface of the zeolite even during He treatment. After oxygen treatment a single peak appeared at T_{max} = 110°C (curve e), and simultaneously, the CO chemisorption diminished. On the other hand, the TPR spectrum for Ru–Co/NaY[**II**] after He treatment (curve f) displays a two-peak spectrum which, after oxidation, featured a different curve (curve g) from that observed for Ru–Co/NaY[**I**], but here the ruthenium was probably retained in the zeolite supercage.

Consequently, if cobalt reducibility is considered, it increases in the sequence $NaY < SiO_2 < Al_2O_3$, while for ruthenium the order is $Al_2O_3 < NaY < SiO_2$.

The estimated average metal particle size, calculated from the dispersion displayed in column 6 in Table 2, is about 1–2 nm assuming spherical metal particles (27). This is in agreement with the XRD data which point to the presence of X-ray amorphous ruthenium particles (43).

3.2. Sample Characterization by X-Ray Photoelectron Spectroscopy

As the TPR studies demonstrated, the structure of the catalysts, i.e., particle size, reducibility, and formation of bimetallic particles, is greatly affected by the pretreatment. Similarly to Pt–Co/NaY samples (25), XPS studies were performed on Ru/NaY, Co/NaY, and Ru–Co/NaY ([**I**] and [**II**]) samples.

3.2.1. Reference and differential charging. Choosing proper references for ruthenium is quite difficult, because its most intense line overlaps with the C1*s* line, a commonly used reference. This is further aggravated by differential charging effect whenever the ruthenium cluster size exceeds a certain limit, which means that true binding energies cannot be referenced to support materials either. This is supported by Wellenbüscher *et al.* (36), while Pedersen and Lunsford did not report this phenomenon (34).

Since we observed such differential charging when the surface was treated with oxygen, we wanted to clarify this aspect experimentally. The NaY support alone, without treatment, pure ruthenium metal powder and a physical mixture of NaY support and ruthenium powder were measured by XPS after reduction in hydrogen at 450°C for 1 h. When metallic powder was reduced, the Ru3*p* line appeared at 461.6 eV (referenced to E_f of metal), close to the expected value for metallic ruthenium, while the Ru3*p* line for the Ru + NaY physical mixture after reduction appeared at 460.2 eV if referenced to Si2*p* and at 461.6 eV if referenced to E_f of ruthenium metal. Except for the Ru3*p* line, the other components Al2*p* (74.4 eV) and O1*s* (532 eV) were as expected when referenced to the Si2*p* line. From this we conclude that larger ruthenium particles exhibit

differential charging. We consistently observed this phenomenon, irrespective of the support when treated in oxygen. In the NaY system a value of 102.7 eV for the Si2*p* binding energy was applied (34, 44) in view of the extensive use of this binding energy, in contrast to the value of 103.4 eV reported for the Si2*p* line for ZSM5 (45).

3.2.2. Ru/NaY zeolite sample. Ru/NaY samples were subjected to sequential treatments in various gas atmospheres, in order to obtain information about the creation, stability, and location of the ruthenium particles. XPS data are presented in Table 3. The Ru3*p* peak appeared at 463.7 eV for the ion-exchanged sample (denoted by as-received) in Table 3, row 1, which value was assigned to $Ru(NH_3)_6^{3+}$ ions. Pedersen *et al.* characterized the $Ru(NH_3)_6^{3+}$ complex and the Ru3*d* line appeared at 282.9 eV in agreement with our results (34).

When the Ru/NaY precursor was calcined *in situ* in oxygen (Table 3, row 2), the Ru3*p* line appeared at 461.9 eV, and the surface concentration of ruthenium (I_{rel} = Ru3*p*/Si2*p* which is denoted from now on as Ru/Si) diminished to one-fourth of that measured in the as-received state. During direct *in situ* calcination ruthenium migrated to the outer surface of the zeolite and likely formed large oxide particles as illustrated by the low Ru/Si ratio. Similar results were obtained in *ex situ* direct oxidation/*in situ* reduction treatments (Table 3, rows 3 and 4). These are in agreement with the TPR and XRD data.

Having confirmed that ruthenium particles migrated and agglomerated when the $Ru(NH_3)_6^{3+}$/NaY sample had been calcined in O_2, the as-received sample was treated in He (Table 3, row 5) and further studied by subsequent *in situ* treatments as shown in rows 6 to 10. After *ex situ* treatment in He at 300°C, the Ru3*p* line appeared at 463 eV which was slightly lower than that recorded for the as-received sample. No nitrogen was detected, thus proving that the $Ru(NH_3)_6^{3+}$ complex had decomposed. There was no significant change in the Ru/Si ratio, indicating that there was no migration of ruthenium to the external surface of the zeolite (compare rows 1 and 5).

In situ reduction of the He-treated sample resulted in the lowering of the binding energy of the Ru3*p* line to 461.8 eV. This value was higher than expected for metallic ruthenium and was assigned to the formation of small metallic particles inside NaY (33) and no significant change in the Ru/Si ratio was observed (Table 3, row 6).

When the reduced sample was oxidized *in situ* at 300°C (Table 3, row 7), the Ru3*p* line appeared at 462 eV, and the Ru/Si ratio also became higher. This increase could be attributed to migration of some of the ruthenium to the external surface of NaY. After subsequent reduction the Ru/Si ratio on the surface also continued to increase and the Ru3*p* line shifted toward 460.4 eV (Table 3, row 8). This low binding energy was attributed to differential charging of the surface because this value was much below that characteristic of ruthenium in the zero oxidation state (461.2 eV). It was assumed that the ruthenium particles very likely lost direct contact with the zeolite, although the increase in the Ru/Si was indicative of ruthenium particles having been spread on the surface during reduction. During oxidation/reduction cycles, the O/Si ratio follows the sequence of treatments.

In the second oxidation/reduction cycle (Table 3, rows 9 and 10) a drop in the Ru/Si ratio was observed after oxidation due to formation of oxide particles from the dispersed metallic ruthenium particles and may be accompanied by further migration from the NaY zeolite. In the subsequent reduction the Ru/Si ratio on the surface increased again. Hence, in addition to reduction of larger RuO_x particles, smaller metallic particles were also formed during reduction.

Comparing the Ru/Si ratios measured in direct oxidation (0.11) with those obtained in He/H_2 treatments (0.34) and in subsequent oxidations (0.48 and 0.34), it must be assumed that the migration is kinetically controlled. To decide upon whether it is true or not we repeated the treatments described in Table 3, rows 5–7, except that calcination lasted for a period of 12 h. The XPS results presented in Table 3, rows 11 and 12, show that the Ru/Si ratio became much larger (0.64) than that observed after the first oxidation (0.48) of a shorter duration. In the subsequent reduction the binding energy of the Ru3*p* line decreased to 460.4 eV, but there was no significant increase in the ruthenium concentration, as observed for the previous set of *in situ* experiments.

3.2.3. Co/NaY sample. The results of the sequential $He/H_2/O_2/H_2$ treatment for Co–NaY catalysts are presented in Table 4. There was no significant binding

TABLE 3

XPS Data of Ru/NaY

Treatment	Ru3*p*	O1*s*	Comment
As-received	463.5 (0.40)	532.0 (4.97)	
$300/O_2/2$	461.9 (0.11)	532.0 (4.91)	*In situ*
Direct oxidation followed by *ex situ* oxidation/*in situ* reduction			
$300/O_2/2$	462.0 (0.08)	532.1 (5.03)	*Ex situ*
$450/H_2/2$	460.3 (0.09)	532.1 (4.69)	*In situ*
Ex situ He treatment followed by *in situ* reduction/oxidation			
300/He/2	463.0 (0.33)	532.1 (5.21)	End of He treatment
$450/H_2/2$	461.8 (0.34)	532.1 (4.60)	
$300/O_2/2$	462.0 (0.48)	532.0 (5.15)	
$450/H_2/2$	460.4 (0.60)	532.1 (4.40)	
$300/O_2/2$	461.2 (0.34)	532.1 (5.01)	
$450/H_2/2$	460.1 (0.49)	532.1 (4.50)	
Ex situ ($He/H_2/O_2$) treatment and subsequent *in situ* reduction			
$300/O_2/12$	462.1 (0.64)	532.2 (5.25)	End of O_2 treatment
$450/H_2/2$	460.4 (0.59)	532.1 (4.55)	

Note. Binding energy in eV; I_{rel} in parentheses. Si2*p*, 102.7 eV; I_{rel}, 1.00; Cl2*p*, 199.10 eV; I_{rel}, 0.16; N1*s*, 400.7; I_{rel}, 0.36.

TABLE 4

XPS Data of Co/NaY

Treatment	Co2*p*	O1*s*
As-received	782.7 (0.52)	532.1 (5.51)
300/He/1	782.9 (0.26)	532.1 (4.79)
450/H_2/2	782.4 (0.26)	532.0 (4.83)
300/O_2/2	782.4 (0.32)	532.0 (4.68)
450/H_2/2	782.6 (0.21)	532.1 (4.79)

Note. Binding energy in eV; I_{rel} in parentheses. Si2*p*, 102.7 eV; I_{rel}, 1.00.

energy shift between the as-received samples and those treated *ex situ* in He; however, the amount of cobalt on the surface decreased to half its initial value. We also saw a parallel decrease in the measured O1*s* line. This may be due to the migration of cobalt ions into the zeolite matrix. Further reduction of the calcined surface revealed a small decrease in the binding energy, but the surface was mostly in the oxidized state. Further oxidation/reduction did not cause any significant change in intensity or in binding energy.

*3.2.4. Ru–Co/NaY[**I**] sample.* The results of the XPS measurements of the Ru–Co/NaY[**I**] sample are presented in Table 5. After treatment in He, the Ru3*p* and Co2*p* binding energies appear at 463.0 and 782.8 eV (Table 5, row 2), respectively. There was no significant change in the amount of ruthenium and cobalt on the surface. The observation of ruthenium in the Ru–Co/NaY[**I**] sample was in line with pure Ru/NaY (Table 3), but cobalt ions appeared not to migrate contrary to Co/NaY (Table 4).

Subsequent reduction in hydrogen (Table 5, row 3) led to a decrease in binding energy of the Ru3*p* line, while Co2*p* remained unchanged. The surface concentration of ruthenium, cobalt, and sodium decreased significantly, while subsequent oxidation (row 4) reversed the situation except for cobalt whose concentration remained the same. Comparing the cobalt concentration in the as-received state and after the first oxidation, it was reduced to half its initial value. The Ru3*p* peak appeared at 462.2 eV and the Co2*p* peak appeared at 782.6 eV. These values are the same as those measured for monometallic NaY-supported samples.

TABLE 5

XPS Data of Ru–Co/NaY[I]

Treatment	Ru3*p*	Co2*p*	O1*s*
As-received	463.5 (0.39)	783.5 (0.18)	532.1 (5.35)
300/He/1	463.0 (0.33)	782.8 (0.14)	532.1 (5.14)
450/H_2/2	462.0 (0.22)	782.6 (0.09)	532.1 (4.92)
300/O_2/2	462.2 (0.63)	782.6 (0.09)	532.1 (5.60)
450/H_2/2	460.4 (0.71)	782.4 (0.10)	532.1 (5.06)

Note. Binding energies in eV; I_{rel} in parentheses. N1*s*, 298.1; Si2*p*, 102. 7 eV; I_{rel}, 1.00.

When cobalt ions exchanged first in zeolite, ruthenium did not affect the reducibility of the cobalt ions. When the oxidized surface was rereduced (row 5), a slight increase in the Ru3*p* intensity on the surface was observed along with a decrease in the binding energy (460.4 eV), well below that of metallic ruthenium (Ru3*p*: 461.2 eV). The ruthenium in the Ru–Co/NaY[**I**] sample is very similar to that of Ru/NaY.

*3.2.5. Ru–Co/NaY[**II**] sample.* In the Ru–Co/NaY[**II**] sample, the first and most striking feature is the reducibility of cobalt ions (Table 6). In contrast to the Ru–Co/NaY[**I**] and Co/NaY samples, here Co^{2+} ions were reduced to a large extent. The second key observation was the diminished migration of ruthenium to the surface but without significant agglomeration/volatile evaporation of RuO_x, resulting in the smallest changes in the Ru/Si intensity ratio during the treatments.

During direct oxidation of Ru–Co/NaY[**II**], a mixing of ruthenium and cobalt became evident indicated by the opposite direction of the intensity change of Ru/Si and Co/Si (Table 6; compare rows 1 and 2). The Ru3*p* binding energy values are the same as those measured for the first oxidation process in all the cases.

The variation in the binding energy of Ru3*p* in the *in situ* $He/O_2/H_2$ studies (Table 6, rows 8 to 13) is the same as that observed for Ru–Co/NaY[**I**] and Ru/NaY. During the H_2 treatment Ru^{3+} ions were reduced to the metallic state and oxidized during calcination in oxygen. In contrast to the Ru–Co/NaY[**I**]–Ru/NaY samples, in the Ru–Co/NaY[**II**] systems ruthenium migration was not observed, at least not to the same extent. After a small initial increase in the Ru/Si ratio during He treatment (compare rows 1 and 8), it remained constant until the second hydrogen treatment. During the second oxidation, the surface concentration of the Ru/Si ratio decreased (row 12), in line with the behavior of Ru/NaY which was attributed to the agglomeration of RuO_x particles. A subsequent small increase in the Ru/Si ratio (Table 6, row 13) might be due to the formation of smaller ruthenium metal particles during reduction. A decrease in the Ru3*p* binding energy of 1 eV was also evident for the Ru–Co/NaY[**II**] sample when the surface after reduction was treated with oxygen.

In the *ex situ* He treatment followed by subsequent reduction–oxidation processes (Table 6, rows 4–7), the states of ruthenium were quite comparable with the *in situ* states except for the ruthenium concentration. We have no explanation for this variation, except that ruthenium migration may be very sensitive even to slight variations in the treatment conditions.

In the as-received state, the Co2*p* line appeared at 781.7 eV (Table 6, row 1) which was substantially less than the values obtained for Ru–Co/NaY[**I**] and Co/NaY. Hence, cobalt appeared to exist in a different environment. The Co/Si ratio on the surface was also much higher. This clearly meant that Co^{2+} ions were topographically at different sites

TABLE 6

XPS Data of Ru–Co/NaY[II]

Treatment	Ru3*p*	Co2*p*	Co^0	CoO	Co^{2+}	O1*s*
As-recieved	464.0 (0.51)	781.7 (2.28)	—	—	781.7	532.1 (4.79)
		Direct oxidation				
300/O_2/2	463.1 (0.64)	782.0 (1.41)	—	779.3	782.2	532.1 (5.03)
400/H_2/2	460.5 (0.63)	777.2 (1.50)	777.5	780.1	782.4	532.1 (4.70)
		Ex situ He treatment followed by *in situ* reduction/oxidation				
300/He/2	462.9 (0.28)	782.3 (0.95)	—	—	782.1	532.1 (4.59)
400/H_2/2	461.5 (0.23)	777.3 (1.11)	777.5	779.5	782.1	532.1 (3.91)
300/O_2/2	462.6 (0.37)	779.7 (1.35)	—	779.6	781.8	532.0 (4.94)
400/H_2/2	460.6 (0.32)	777.4 (1.34)	777.5	779.9	781.9	532.0 (4.0)
		In situ He/O_2/H_2 treatment				
300/He/2	463.0 (0.65)	781.6 (2.44)	—	—	781.7	531.8 (4.66)
400/H_2/2	461.3 (0.42)	777.9 (1.4)	778 (0.80)	781.8		532.0 (4.22)
300/O_2/2	463.0 (0.37)	780.0 (1.55)	—	779.9	782.5	532.0 (5.11)
400/H_2/2	460.4 (0.43)	777.4 (1.41)	777.5 (0.7)	780	781.7	532.1 (4.17)
300/O_2/2	462.9 (0.12)	779.4 (1.35)	—	779.4	781.7	531.9 (4.8)
400/H_2/2	460.4 (0.28)	777.2 (1.45)	777.4 (0.6)	780	782	532.0 (4.18)
		In situ He/O_2/H_2 treatment using XSAM 800 cpi				
As-received	464.1 (1.1)	781.7 (4.10)	—	—	781.7	531.9 (7.86)
300/He/2	461.9 (1.08)	781.6 (4.10)	778.2 (0.1)	782.1		531.9 (6.44)
400/H_2/2	461.8 (0.80)	777.9 (1.87)	777.9 (0.6)	781.3		531.9 (6.25)
300/O_2/2	463.5 (0.94)	780.0 (3.00)	—	779.6	781.3	531.7 (7.41)
400/H_2/2	460.9 (0.91)	777.4 (3.06)	777.8 (0.4)	780	781.6	531.8 (6.17)

Note. Binding energies in eV; I_{rel} in parentheses. Si2*p*, 102.7 eV; I_{rel}, 1.

(outer shell). However, the picture of Co2*p* was somewhat different as shown in Fig. 3c. Although there was no significant difference in the binding energy between the as-received and oxidized states, the FWHM was significantly higher for the latter sample. About 80% of this broad Co2*p* peak was assigned to the state appearing at 782.2 eV binding energy with shake-up satellite, while the rest was associated with a state appearing at 780 eV binding energy without shake-up satellite. Subsequent reduction led to the appearance of a Co2*p* line at 777.2 eV (Fig. 4d) in which 60% of the cobalt was in the metallic state.

During He treatment the Co2*p* binding energy and the Co/Si ratio on the surface did not show significant variation, implying the absence of significant variation in the cobalt environment or in migration. During the first hydrogen treatment the Co2*p* line centered at 777.9 eV, the cobalt concentration on the surface dropped (Table 6, row 9) and the subsequent oxidation/reduction cycle had no significant effect on cobalt concentration. At least 80% of the cobalt was reduced to the metallic state with significant migration. In subsequent oxidation all the cobalt was oxidized, and the Co2*p* binding energy shifted toward 780 eV without any satellite structure; only a small amount of the Co2*p* line appeared at 782 eV with satellite. During subsequent reduction, the metallic Co2*p* contribution was only 70% (Table 6, row 11). Oxidation of the twice-reduced surface gave a similar picture to that of first oxidation (Figs. 3a and 3b). The third and final reduction also leads to metallic cobalt, but to a lesser extent. The varying degree of cobalt reducibility during this reduction/oxidation cycle is clearly evident in Figs. 4a–4c.

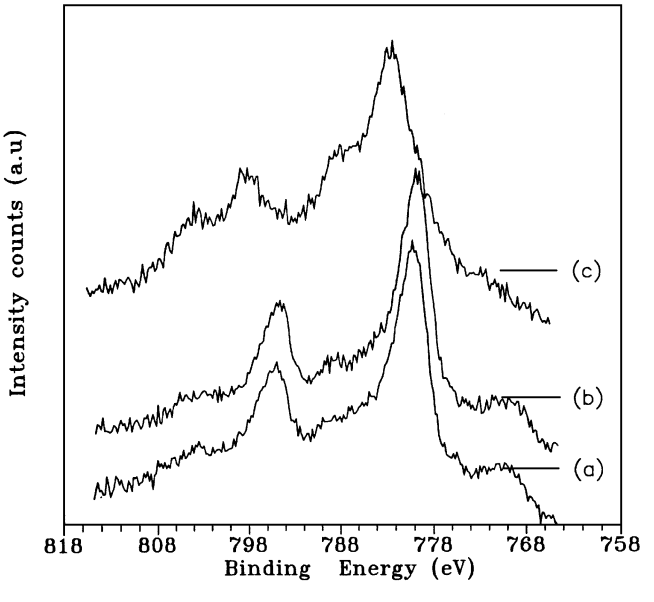

FIG. 3. XPS spectra of Co2*p* after oxidation. (a) He treated/reduced Ru–Co/NaY[**II**] samples after first oxidation; (b) after reduction of (a) and second oxidation; (c) after direct oxidation (oxidation/reduction is at 300°C/400°C, respectively).

During the *ex situ* He treatment the Co/Si ratio was much lower than that measured in the sample treated *in situ* (compare Table 6, rows 4 and 8), while the subsequent reduction/oxidation led to a comparable cobalt concentration. As shown in the *in situ* experiments, reduction led to a mixed state with peak maxima at 777.4 eV and with 60% of the cobalt in the metallic state. This result is quite different from the first reduction process observed for the *ex situ* studies but comparable to the second reduction after oxidation. Subsequent treatment in oxygen led to the appearance of the Co2*p* line at 779.7 eV without a significant satellite structure. Hence, the state of cobalt under *ex situ* and *in situ* conditions are comparable.

Since Co^{2+} ions could not be reduced in the Ru–Co/NaY[**I**] and Co/NaY samples, we confirmed this in the Ru–Co/NaY[**II**] sample by carrying out an independent *in situ* experiment using in XSAM800cpi equipment. The data presented in Table 6 and plotted in Fig. 5 differed in two respects while confirming the reducibility of Ru^{3+} and Co^{2+} ions: these ions were reduced, at least partially, during the He decomposition step. Subsequent treatment in hydrogen reduced only 60% of the Co^{2+} ions compared to 80% in the earlier experiment.

3.2.6. Transmission electron microscopic studies. Ru/NaY and Ru–Co/NaY[**II**] samples were measured by TEM at 400,000 magnification after reduction in hydrogen. Due to technical reasons the conditions of the treatment differed slightly from those of the He treatment. Figures 6a and 6b show the TEM pictures after hydrogen treatment of Ru/NaY and Ru–Co/NaY[**II**]. The presence of Ru particles in Ru/NaY was proven by EDX; they had uniform size distribution of 2–3 nm (Fig. 6a). For Ru–Co/NaY[**II**] both ruthenium and cobalt were in the zeolite cage and seemed to be uniform and amorphous with particle size of 3–4 nm (Fig. 6b). In both cases large particles were also found, but their ratio could not be determined.

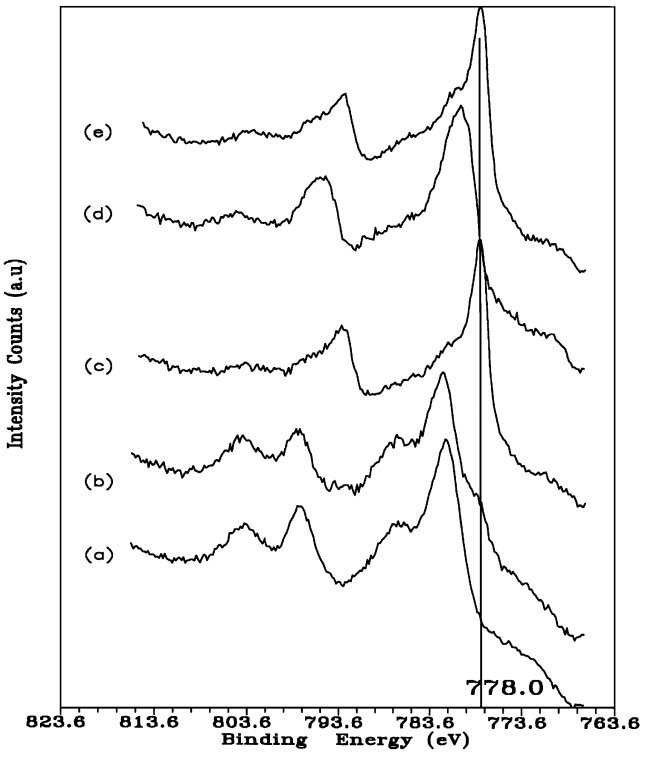

FIG. 5. XPS spectra for *in situ* treatments of Ru–Co/NaY[**II**] samples. (a) as-received; (b) He treatment of sample (a); (c) reduction of sample (b); (d) oxidation of sample (c); (e) reduction of sample (d).

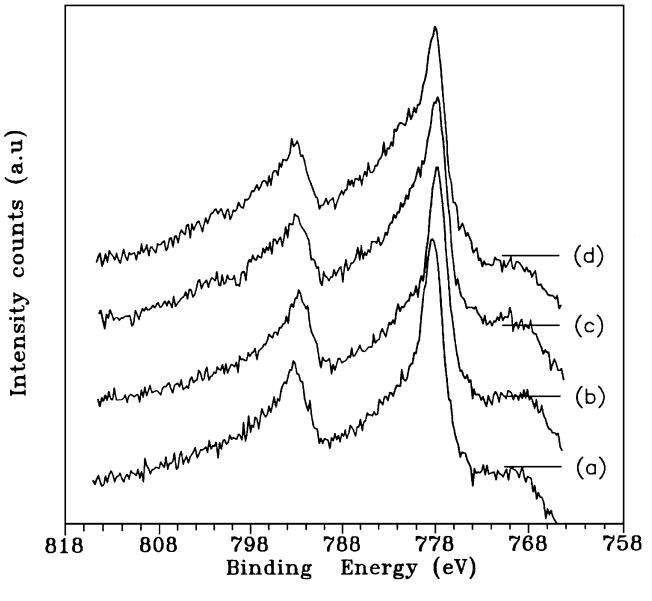

FIG. 4. XPS spectra of the *in situ* treated Ru–Co/NaY[**II**] samples in the Co2*p* spectral region. (a) reduced sample after He treatment; (b) after first oxidation/reduction of (a); (c) after second oxidation/reduction of (a); (d) after direct oxidation/reduction.

4. DISCUSSION

In order to understand how the active metal sites were generated from metal ions deposited on various supports, particularly on NaY zeolite, the genesis of metal catalysts was studied. This is particularly important in bimetallic systems, because the presence of two metals does not necessarily result in alloy formation. Nevertheless, metallic contacts may facilitate reduction of metal ions and/or stabilization of small metal particles. For Co/Al_2O_3 (46) and $Pt–Co/Al_2O_3$ (47) the studies described here resulted in a better understanding of the structure–activity relationships.

One of the most intriguing results that we obtained from studying the ruthenium–cobalt support systems is the establishment of a reducibility sequence for one metal on various supports. TPR disclosed that the reducibility of cobalt increases in the order $NaY < SiO_2 < Al_2O_3$, while

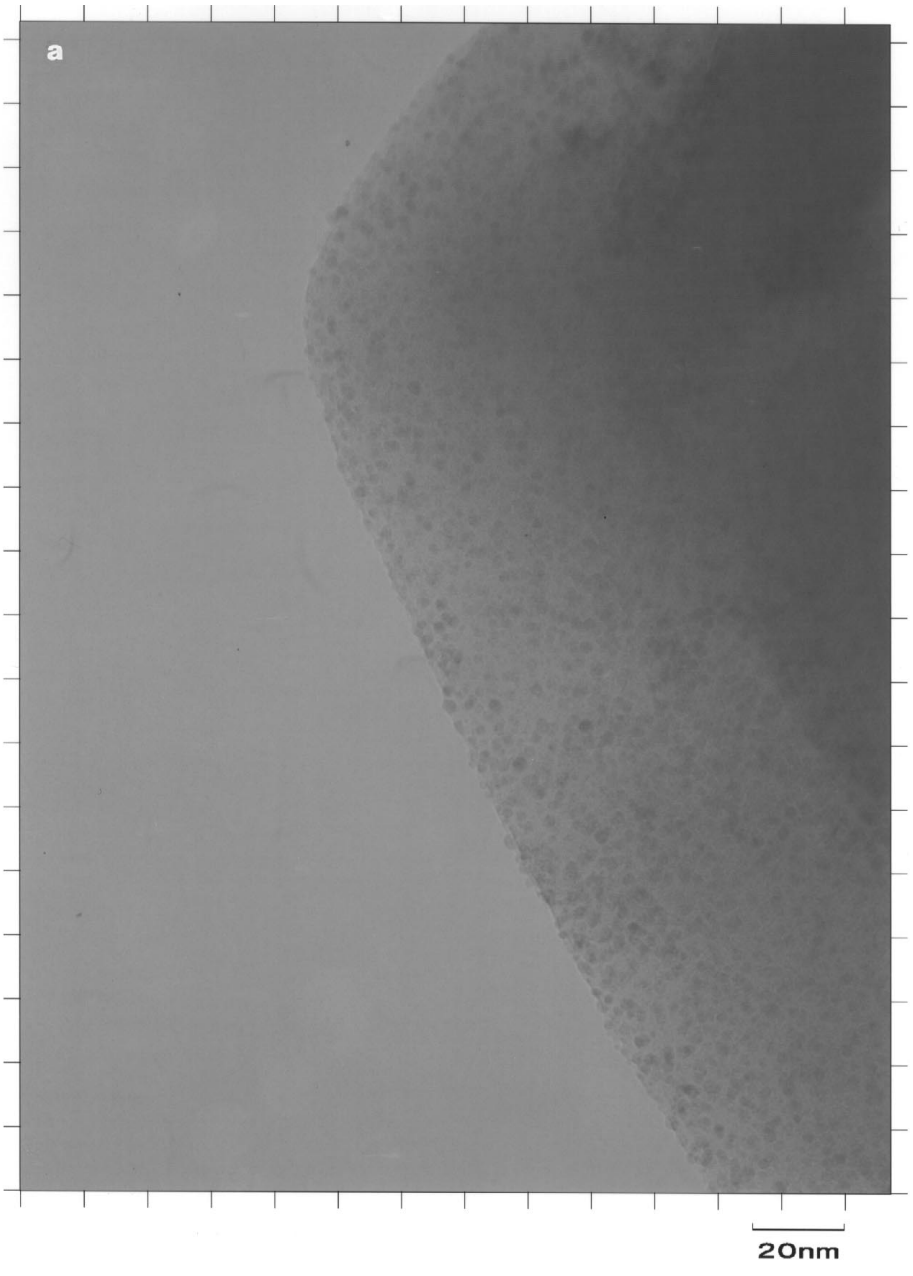

FIG. 6. HRTEM picture of Ru/NaY (a) and Ru–Co/NaY[**II**] (b) samples using magnification of 400,000.

for ruthenium a sequence of $Al_2O_3 < NaY < SiO_2$ was observed. As will be illustrated in the accompanying paper the sequence of reducibility plays important role in the low-temperature dissociative methane chemisorption carried out under oxygen-free conditions (48).

The sequence of reducibility observed can be interpreted as follows. Co/NaY is partially reducible only above 600°C (24). On alumina, a cobalt surface phase forms (40) which is reducible above 400°C, whereas on Co/silica a stable, barely reducible silicate phase is present. Since the metal/support interaction for ruthenium is weaker, hydrogenation of the impregnated and calcined phases produces more metal particles.

The most remarkable part of the present studies concerns the mechanism of the creation of metallic and bimetallic particles located in the NaY zeolite system. Ru/NaY, Co/NaY, and Ru–Co/NaY[**I**] and [**II**] indeed behave in a completely different manner with regard to the genesis of metal particles. Ruthenium is known to migrate as well as to form larger particles during direct oxidation on a variety of supports. In addition, some of the oxide phases are volatile. Pedersen and Lunsford (34) observed enrichment of

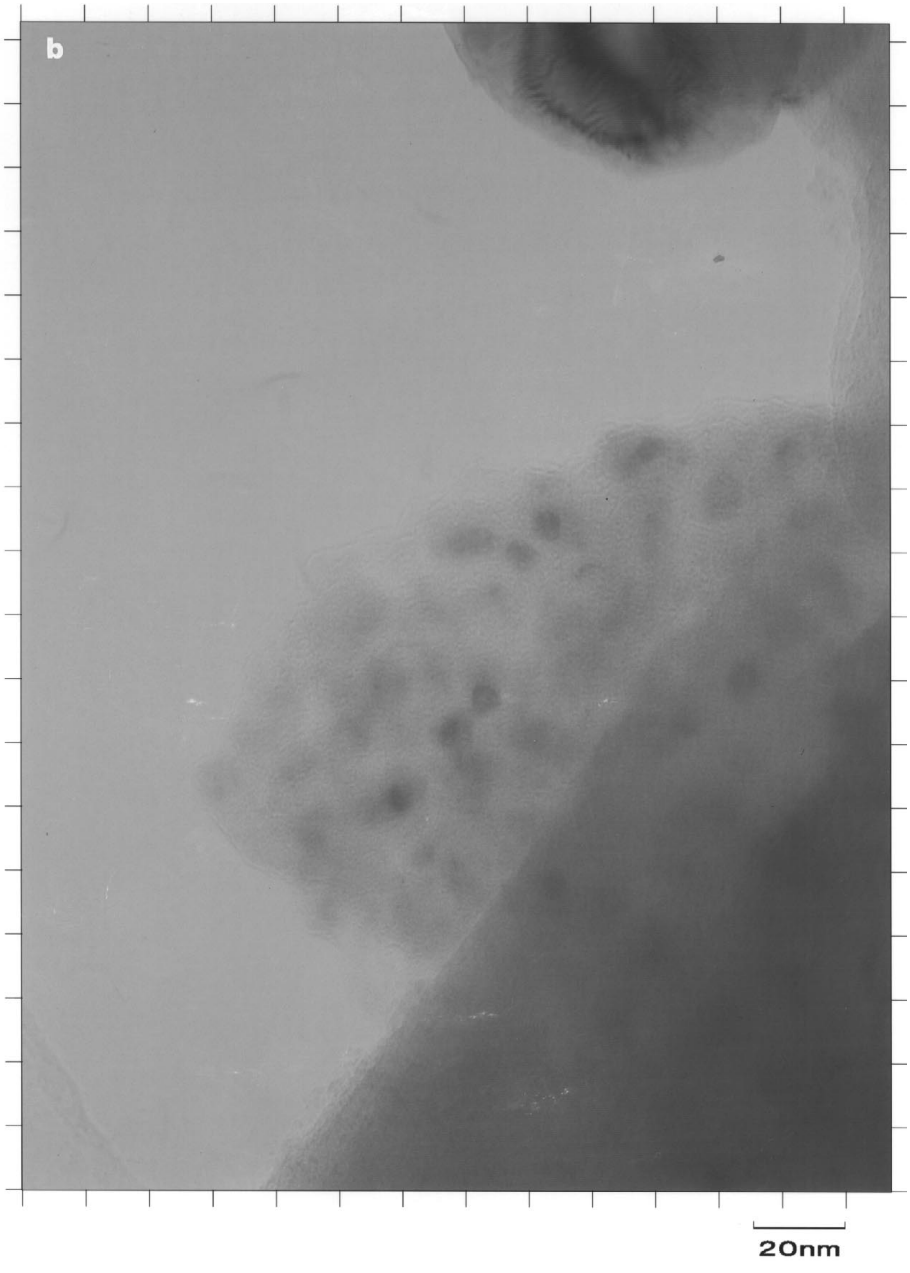

FIG. 6—*Continued*

ruthenium estimated by XPS during oxidation at 400°C for 2 h, but apparently there was no agglomeration. Recently, Zou and Gonzalez studied the dispersion of Ru/SiO_2 during oxidation followed by reduction (35). Their electron microscopic studies indicated the formation of large particles during oxidation at 250°C.

In our experiments direct oxidation and subsequent reduction leads to large metal particles as indicated by a low Ru/Si ratio. A several fold decrease in the Ru3*p* intensity on the surface and lower binding energy after oxidation result from the formation of larger RuO_x, or after reduction ruthenium particles on the surface, at least for Ru/NaY and Ru–Co/NaY[**I**]. The large ruthenium particles formed have differential charging on the surface and hence appear at lower binding energy. The differential charging is well evidenced from the binding energy of ruthenium particles after reduction which are well below those measured in the metallic state. In our experiments, the Ru3*p* line in a mixture of metallic ruthenium particles and NaY could not be referenced to Si2*p* to obtain true binding energy. In the case of Ru–Co/NaY[**II**], however, differential charging was not observed; the Ru3*p* intensity on the surface did not

diminish appreciably. This may be due to the presence of cobalt ions located around the pore mouth that hamper the agglomeration of the ruthenium particles when Co^{2+} ions are exchanged on $[Ru(NH_3)_6]^{3+}$/NaY sample.

In contrast to direct oxidation, where a complete agglomeration is the case for all particles except for Ru–Co/NaY[**II**], indirect oxidation (after He/H_2 treatment) led to entirely different surfaces in all cases. This route is certainly much more favorable than direct oxidation. This is well proven by the increase in the ruthenium surface concentration after identical reduction process. During the second reduction after the first calcination of the reduced surface in oxygen, moderately large particles are formed and could be reduced to smaller metallic particles as demonstrated by Zou and Gonzalez (35).

The ruthenium cluster morphology cannot be established without a doubt from the present results alone. However, we can conclude that the migration of ruthenium to the outer surface and agglomeration take place in two independent steps, the first being migration to the surface and the second agglomeration. The increase in the ruthenium concentration on the surface during the second oxidation process is due to kinetically controlled ruthenium migration. This means that only a part of the ruthenium could migrate during the first oxidation process, while the rest migrated only in the second. This is proven by the comparable ruthenium concentration in single step *ex situ* oxidation of longer duration (Table 3, row 11). In view of the longer oxidation process, not only could all the mobile ruthenium have migrated, but it could also have agglomerated to quite large particles, shown by the stable number of estimated metallic ruthenium particles during reduction. This surface, however, differs completely from the directly oxidized surface.

There is, however, another important reason for this occurrence. In direct oxidation of $[Ru(NH_3)_6]^{3+}$/NaY and oxidation of small metal particles inside the supercage of NaY, two different processes take place. In the first case, Ru^{3+} ions are atomically dispersed and can move fast immediately to the outer layer of the zeolite, whereas oxidation of the small metal particles which fill up the supercage, is a surface-controlled reaction which takes time. Furthermore, if the migration process is hampered by Co^{2+} ions preferentially located near the pore mouth (at least in the Ru–Co/NaY[**II**] sample), not only the migration of ruthenium, but also their agglomeration is retarded. When $[Ru(NH_3)_6]^{3+}$ ions are located in the outer layer or no cobalt ions are in the system, the migration process is freely performed resulting in the formation of large ruthenium particles.

It is difficult to explain all the variation in the ruthenium concentration in indirect oxidation studies on Ru–Co/NaY[**II**] in which results of *ex situ* and *in situ* studies of the same treatment differed significantly.

As far as cobalt is concerned, in the case of Co/NaY and Ru–Co/NaY[**I**], there is no significant variation in the nature of cobalt on the surface, because Co^{2+} ions are irreducible, although migration properties differ slightly. The status of cobalt changes only slightly in the direct and indirect redox cycles. However, in Ru–Co/NaY[**II**] cobalt ions differ from those in other samples because Co^{2+} ions were reduced to a large extent. The reducibility of Co^{2+} ions may have occurred for one of the following reasons: either because of diminished interaction with the support, in view of the exchange over Ru/NaY, or because of the impact of the ruthenium metal. The latter is much more convincing considering the lower differential charging for ruthenium and the oxidized surface (80%) and the smaller agglomeration during direct oxidation.

The H_2/O_2 treatment makes a lesser amount of Co^{2+} ions reducible. This is clear from the fact that 80% of the Co^{2+} ions is reducible during the first reduction and almost 60% in subsequent reductions. This is also clearly indicated by the shapes of the peak of the reduced sample. After direct oxidation, only 60% of the sample was in the metallic state, and a small but only significant shift in the cobalt binding energy could possibly be due to the change in particle size. The reducibility of cobalt ions in the repeated oxidation/reduction cycles is clear evidence of the formation of bimetallic particles.

The nature of the cobalt on the surface in the direct and indirect oxidation processes differed significantly. The former is constituted by the oxidized cobalt with a corresponding satellite structure, while the latter exhibited no satellite structure. In both cases, no measurable metallic cobalt is detected.

TPR, XRD, and TEM measurements fully support the scenario depicted above. As shown in Table 2, He treatment followed by reduction in hydrogen always resulted in small particles as calculated from CO chemisorption supported by TEM. The particle sizes are in the range of 1–3 nm using a model of spherical particles (27), which is in line with XRD results showing amorphous ruthenium metal particles and the TEM picture presented here. Oxidation led to the formation of large RuO_x particles patterned in the XRD measurements and with a dramatic decrease in CO chemisorption on the metal particles formed after reduction. These results are also supported by recent results (49, 50).

It is worth considering why the reduction of cobalt ions as well as the retarded migration of ruthenium particles are affected by the sequence of ion exchange. As is known, in the ion-exchange process some of the ions first exchanged are removed during the second exchange process. Consequently, the structure of the zeolite containing two different ions is a "cherry" type, as has been shown in the Pt–Co/NaY system (25) and recently by other authors (51). On the other hand, if cobalt is in the inner layer and ruthenium

is in the outer layer, the latter can be more easily removed via migration to the external surface of the NaY zeolite than in the case of reverse sequence of exchange. Thus, when ruthenium is removed from the neighborhood of cobalt, Co^{2+} ions cannot be reduced as is also the case for Ru–Co/NaY[**I**]. Conversely, if ruthenium is exchanged first, its migration is limited by the cobalt in the outer layer; therefore, after ruthenium reduction, the hydrogen activated on the ruthenium surface can migrate easily over cobalt and is reduced to a large extent (Ru–Co/NaY[**II**]). Fixation of ruthenium in the vicinity of cobalt makes the cobalt reducibility easier, as was shown on $Ru–Co/Al_2O_3$ and other ruthenium–cobalt bimetallic systems (52).

5. CONCLUSIONS

Ruthenium migrates and agglomerates to large oxide particles when the precursor is treated directly in oxygen as is the case for Ru/NaY and Ru–Co/NaY[**I**], whereas in the Ru–Co/NaY[**II**] sample migration is restricted due to the presence of cobalt ions. Migration of ruthenium appears to be controlled by a kinetic effect.

The Co^{2+} ions in Co/NaY and Ru–Co/NaY[**I**] are irreducible under all conditions. The reduction of cobalt ions in the Ru–Co/NaY[**II**] sample catalyzed by ruthenium is evident in all circumstances, but the extent of reduction varies.

When large ruthenium particles are present after oxygen treatment, the ruthenium particles have a very weak contact with the support as is the case for Ru/NaY and Ru–Co/NaY[**I**]. For Ru–Co/NaY[**II**] in the oxidized state, the impact of differential charging is reduced, possibly due to bonding through oxygen linked to cobalt.

The ruthenium–cobalt bimetallic phase could be inferred for Ru–Co/NaY[**II**].

ACKNOWLEDGMENTS

The authors are indebted to the European Community for the grant within the scope of the COST Program (COST D5/0001/93) and the National Science and Research Fund (T-022117). We are grateful to Mrs. E. Zsoldos for the XRD and to Dr. Z. Szõkefalvi for XRF measurements.

REFERENCES

1. Rostrup-Nielsen, J. R., *Catal. Today* **18**, 125 (1993) and references therein.
2. Koerts, T., Deelen, M. J. A. G., and van Santen, R. A., *J. Catal.* **138**, 101 (1992).
3. Koerts, T., and van Santen, R. A., *J. Mol. Catal.* **74**, 185 (1992).
4. Koerts, T., and van Santen, R. A., *J. Chem. Soc., Chem. Commun.* 1281 (1991).
5. Koerts, T., Leclerq, P. A., and van Santen, R. A., *J. Am. Chem. Soc.* **114**, 7272 (1992).
6. Guczi, L., van Santen, R. A., and Sarma, K. V., *Catal. Rev. Eng. Sci.* **38**, 249 (1996).
7. Solymosi, F., Erdõhelyi, A., and Cserényi, J., *Catal. Lett.* **16**, 399 (1992).
8. Solymosi, F., Erdõhelyi, A., Cserényi, J., and Felvégi, A., *J. Catal.* **147**, 272 (1994).
9. Erdõhelyi, A., Cserényi, J., and Solymosi, F., *J. Catal.* **141**, 287 (1993).
10. Solymosi, F., and Cserényi, J., *Catal. Today* **21**, 561 (1994).
11. Solymosi, F., and Révész, K., *J. Am. Chem. Soc.* **113**, 9145 (1991).
12. Solymosi, F., and Kovács, I., *Surf. Sci.* **296**, 171 (1993).
13. Solymosi, F., Kovács, I., and Révész, K., *Catal. Lett.* **27**, 53 (1994).
14. Belgued, M., Pareja, P., Amariglio, A., and Amariglio, H., *Nature* **352**, 789 (1991).
15. Belgued, M., Amariglio, H., Pareja, P., Amariglio, A., and Saint-Just, J., *Catal. Today* **13**, 437 (1992).
16. Pareja, P., Amariglio, A., Belgued, M., and Amariglio, H., *Catal. Today* **21**, 423 (1994).
17. Mielczarski, M., Monteverdi, S., Amariglio, A., and Amariglio, H., *Appl. Catal. A* **104**, 215 (1993).
18. Belgued, M., Amariglio, A., Pareja, P., and Amariglio, H., *J. Catal.* **159**, 441 (1996); *ibid* **159**, 449 (1996)
19. Cunningham, R. H., van Santen, R. A., van Grondelle, J., Mangus, A. V. G., and Ijzendoorn, L. J., *J. Chem. Soc. Chem. Comm.*, in press.
20. Koerts, T., van Wolput, J. H. M. C., de Jong, A. M., and Niemantsverdriet, J. W., *Appl. Catal. A* **15**, 315 (1994).
21. Cunningham, R. H., Mangnus, A. V. G., van Grondelle, J., and van Santen, R. A., *Catal. Today* **21**, 431 (1994).
22. Lu, G., Hoffer, T., and Guczi, L., *Catal. Lett.* **14**, 207 (1992).
23. Lu, G., Hoffer, T., and Guczi, L., *Appl. Catal.* **93**, 61 (1992).
24. Lu, G., Zsoldos, Z., Koppány, Zs., and Guczi, L., *Catal. Lett.* **24**, 15 (1994).
25. Zsoldos, Z., Vass, G., Lu, G., and Guczi, L., *Appl. Surf. Sci.* **78**, 467 (1994).
26. Guczi, L., Sarma, K. V., and Borkó, L., *Catal. Lett.* **39**, 43 (1996).
27. Guczi, L., Koppány, Zs., Sarma, K. V., Borkó, L., and Kiricsi, I., "Progress in Zeolite and Microporous Materials" (H. Chon, S.-K. Ihm, and Y. S. Uh, Eds.), in *Stud. Surf. Sci. Catal.* **105**, p. 861. Elsevier, Amsterdam, 1997.
28. Guczi, L., Sarma, K. V., Koppány, Zs., Sundararajan, R., and Zsoldos, Z., *Stud. Surf. Sci. Catal.*, in press.
29. Solymosi, F., and Cserényi, J., *Catal. Today* **34**, 343 (1995).
30. Shyu, J. Z., Goodwin, J. G., Jr., and Hercules, D. M., *J. Phys. Chem.* **89**, 4983 (1985).
31. Ishihara, T., Harada, K., Eguchi, K., and Arai, H., *J. Catal.* **136**, 161 (1992).
32. Alerasool, S., and Gonzalez, R. D., *J. Catal.* **124**, 204 (1990).
33. Gustafson, B. L., and Lunsford, J. H., *J. Catal.* **74**, 393 (1982).
34. Pedersen, L. A., and Lunsford, J. H., *J. Catal.* **61**, 39 (1980).
35. Zou, W., and Gonzalez, R. D., *J. Catal.* **133**, 202 (1992).
36. Wellenbüscher, J., Rosowski, F., Kengler, U., Muhler, M., Ertl, G., Guntow, U., and Schlögl, R., *in* "Zeolites and Related Microporous Materials: State of the Art 1994" (J. Weitkamp, H. G. Karge, H. Pfeifer, and W. Hölderich, Eds.), *Stud. Surf. Sci. Catal.* **84**, p. 941. Elsevier, Amsterdam, 1994.
37. Ishihara, T., Harada, K., Eguchi, K., and Arai, H., *J. Catal.* **136**, 161 (1992).
38. Cho, I. H., Cho, S. J., Park, S. B., and Ryoo, R., *J. Catal.* **153**, 232 (1995).
39. Reuel, R. C., and Bartholomew, C. H., *J. Catal.* **85**, 63 (1984).
40. Zsoldos, Z., Hoffer, T., and Guczi, L., *J. Phys. Chem.* **95**, 798 (1991).
41. Guczi, L., Hoffer, T., Zsoldos, Z., Zyade, S., Maire, G., and Garin, F., *J. Phys. Chem.* **95**, 802 (1991).
42. Zsoldos, Z., and Guczi, L., *J. Phys. Chem.* **96**, 9393 (1992).
43. Anderson, J. R., "The Structure of Metal Catalysts." Academic Press, New York, 1975.

44. Barr, T. L., *in* "Practical Surface Analysis, Volume 1" (D. Briggs and M. P. Seah, Eds.), p. 412. Wiley, New York, 1990.
45. Lemay, G., Kaliaguine, S., Adnot, A., Nahar, S., and Cozak, D., *Can. J. Chem*. **64**, 1943 (1986).
46. Zsoldos, Z., Garin, F., Hilaire, L., and Guczi, L., *Catal. Lett.* **33**, 39 (1995).
47. Zsoldos, Z., Garin, F., Hilaire, L., and Guczi, L., *J. Mol. Catal.* **111**, 113 (1996).
48. Guczi, L., Sarma, K. V., and Borkó, L., *J. Catal.* **167**, 495 (1997).
49. Wellenbüscher, J., Muhler, M., Mahdi, W., Sauerlandt, U., Schütze, J., Ertl, G., and Schlögl, R., *Catal. Lett.* **25**, 61 (1994).
50. Wrabetz, S., Guntow, U., Schlögl, R., and Karge, H. G., "Progress in Zeolite and Microporous Materials" (H. Chon, S.-K. Ihm, and Y. S. Uh, Eds.), *Stud. Surf. Sci. Catal.* **105**, p. 583. Elsevier, Amsterdam, 1997.
51. Boix, A. V., Ulla, M. A., and Petunchi, J. O., *J. Catal.* **162**, 139 (1996).
52. Kogelbauer, A., Goodwin, J. G., Jr., and Oukaci, R., *J. Catal.* **160**, 125 (1996).